AIAA Aviation Forum and ASCEND co-located Conference Proceedings
21 - 25 July 2025, Las Vegas, Nevada
AIAA AVIATION FORUM AND ASCEND 2025

10.2514/6.2025-3651

Investigation of noise emission on the ECL5 fan stage by means of sector LES simulations

A. Beurville *, J. Boudet †, A. Giauque ‡ and V. Clair §
École Centrale de Lyon, CNRS, Université Claude Bernard Lyon 1, INSA Lyon, LMFA, UMR5509, 36 Avenue Guy de Collongue, 69130, Écully, France

In the present study, the broadband noise of an ultra-high bypass ratio fan/OGV stage, developed at École Centrale de Lyon, is analyzed. Wall-modeled large eddy simulations (LES) over a periodic angular sector have been performed at nominal speed, with a flow in the transonic regime. The noise emissions are directly obtained by the fully compressible LES using a well refined unstructured mesh. The good level of comparison with experimental data motivates a deeper analysis devoted to the acoustic waves within the stage. Upstream of the rotor blades a low frequency hump between 750 Hz and 1200 Hz is detected. A dynamic mode decomposition of pressure fluctuations is performed for this frequency range. The decomposition suggests that the modal structure of this low frequency noise emission corresponds to the first radial mode, and is homogeneous in the azimuthal direction. A mode-matching strategy in duct engine is performed to investigate further those acoustic duct modes in the entire stage. This hump is also detected in the inter-stage. The frequency range of the of this modal structure is cut-off downstream of the stator vanes.

I. Introduction

In response to stringent new regulations, aero-engine manufacturers are focusing on optimizing turbofan engines to enhance efficiency and minimize pollutant and noise emissions. Modern and future turbofan engines, such as ultra-high bypass ratio (UHBR) designs, feature larger fan diameters in order to increase the by-pass ration and the efficiency. The noise generated by the fan-OGV stage consists of tonal and broadband components. Tonal noise, which arises from periodic interactions within the fan stage and is influenced by the number of blades and vanes [1], is well-documented in the literature [2]. Broadband noise, stemming from stochastic mechanisms such as turbulence in boundary layers and wakes, is less documented due to its complex nature and the challenge of attenuating it across a wide range of cut-on modes. Several mechanisms contribute to broadband noise, including the interaction of inlet turbulence with rotor blades, vortex noise in the tip region of the rotor [3], trailing edge noise [4], and rotor-stator interaction noise. Additionally, transonic mechanisms come into play when the fan has a large diameter, further complicating the noise generation processes. In fact, these shock-waves will behave as an acoustic rotating source and guide the propagation of outlet guide vanes emissions.

Recent advancements in computing resources have enabled detailed descriptions of turbulent flow in turbomachinery applications through high-fidelity simulations, such as large eddy simulation (LES) and direct numerical simulation (DNS). These simulations can capture the turbulent structures that generate broadband noise. However, DNS remains computationally expensive and is limited to low Reynolds number and academic configurations. Therefore, LES is preferred for its balance of accuracy and computational efficiency in modelling complex flows in a fan stage. Several acoustic investigation using LES for turbomachinery applications were conducted and manage to analyze both tonal and broadband noise [5]. This study employs LES to investigate the broadband noise of an ultra-high bypass ratio (UHBR) periodic fan/OGV stage in a transonic regime.

The main objective of this work is to investigate low frequency noise emissions of a fan/OGV stage in transonic configuration using LES. The paper is organized as follows. Section II presents the fan/OGV stage configuration, the LES numerical parameters and the mesh characteristics. Section III includes a validation of the LES using experimental data, as well as the conducted low frequency investigation.

*PhD student, École Centrale de Lyon, LMFA, allan.beurville@ec-lyon.fr
†Pr., École Centrale de Lyon, LMFA, jerome.boudet@ec-lyon.fr
‡Pr., École Centrale de Lyon, LMFA, alexis.giauque@ec-lyon.fr
§Dr., École Centrale de Lyon, LMFA, vincent.clair@ec-lyon.fr

II. Numerical setup

A. Computational domain

This study focuses on the ECL5 fan/OGV stage, an open test case designed at École Centrale de Lyon [6–8]. This Ultra High By-pass Ratio (UHBR) fan/OGV stage has been investigated during the European CATANA project, in order to provide a multi-physical benchmark representative of near-future UHBR fan concepts. The stage is made of 16 rotor blades and 31 stator vanes.

A representation of the computational domain of the angular sector is provided in Figure 1. The AVBP LES solver used for this study requires the angular extent of the rotor and stator domains to be the same [9]. Therefore, the original configuration with 31 OGVs is adapted to 32 OGVs to allow a $2\pi/16$ angular periodicity. In order to maintain the stage performance, the solidity of the OGV is preserved [10]. In this case, the additional vane decreases the inter-vane spacing, thus the chord is rescaled with a $31/32$ factor. The computational domain extends from 3.5 fan chord lengths upstream of the rotor to 4.5 vane chord lengths downstream of the stator.

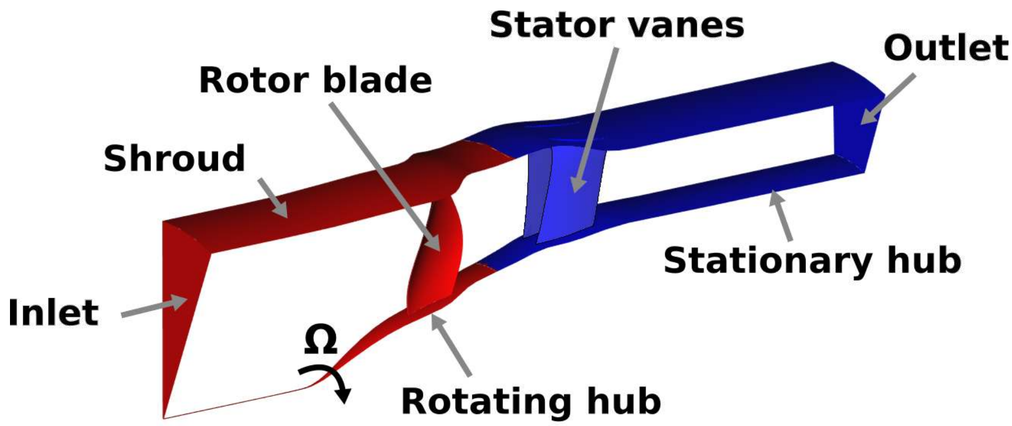

Fig. 1 Computational domain of the ECL5 fan/OGV stage angular sector. The rotor domain (colored in red) and the stator domain (in blue) overlaps over five cells to perform the domain coupling at each time step.

The present simulation is performed at nominal speed, which corresponds to $\Omega = 11,000$ RPM. The operating condition is the design point, with a mass-flow rate of 36 kg·s^{-1} for the full stage configuration and 2.25 kg·s^{-1} for the periodic angular sector. The flow for this operating point is transonic in the rotor domain and a supersonic pocket develops on the suction side of the rotor.

B. LES numerical parameters

In this study, the simulation of the ECL5 fan stage has been performed using AVBP, an explicit unstructured fully compressible LES solver developped by CERFACS [9, 11, 12]. For turbomachinery applications, the resolution is performed over two domains: a rotating domain containing the rotor blades and a static domain containing the stator vanes. Both domains are coupled at each computational time step using a Multi Instance Solver Coupled through Overlapping Grids (MISCOG) third order interpolation [13]. High-performance LES solver is preserved using the CWIPI library developed by ONERA [14]. The rotor domain contains one rotor blade, and the stator domain contains 2 stator vanes.

The scheme used to solve the Navier Stokes equations is a third order in space and time, finite-volume, convective scheme : the Two-steps Taylor Galerkin C scheme (TTGC) [15]. The SIGMA sub-grid scale model [16] is used to model the unresolved eddies. Non-reflecting Navier-Stokes Characteristic Boundary Conditions [17] (NSCBC) are used at both the inlet and the outlet. The inflow is uniform, purely axial, with a total pressure of P_0 =101,325 Pa and a total temperature of $T_0 = 288.15$ K. The desired mass-flow rate is obtained by adjusting the section-averaged static pressure at the outlet boundary condition. Periodic boundary conditions are applied on the azimuthal boundaries of the computational domain. A wall function [18] is used to model the inner part of the boundary layers, and reduce the computational cost. This modelisation is applied for each wall surface: the rotor blade, the stator vanes, the shroud, and the hub. The dimensionless velocity relative to the wall evolves linearly for $y^+ < 11.45$ and a log-law is used otherwise : $u^+ = 1/\kappa \ln(Ay^+)$, with $\kappa = 0.41$ and $A = 9.2$. The shock-waves are handled using Cook and Cabot [19] model. Ducros and Bhagatwala limiters [20, 21] are applied in order to limit the contribution of the Cook artificial bulk viscosity in regions of interest (vorticity and positive dilatation regions respectively).

The time-step for the simulation is set to $\Delta t = 1.65 \cdot 10^{-8}$s in order to preserve the Courant-Friedrichs-Lewy number below 0.7 everywhere in the computational domain. The computational cost of the LES simulation is around 192,000 CPUh per rotation. Four entire rotations of the fan are performed for the numerical and statistical convergence. Twelve additional fan rotations are used for the acoustic data collection and post-processing.

C. Mesh characteristics

Simulations has been performed on a hybrid unstructured mesh. The mesh contains approximately 100 millions cells. Prisms are used near the walls in order to handle the boundary layers and tetrahedra are used everywhere else. The mesh characteristic sizes and properties are chosen in a way to ensure a suitable resolution of the boundary layers and wakes resolve a part of the inertial spectrum, and also to propagate the acoustic waves in the fan stage without significant dissipation and dispersion errors.

The dimensionless wall-normal distance y^+ of the first prismatic layer is lower than 35 on the blade and vane skins. A stack of 11 prisms layers is used in order to handle the boundary layers. The prism height is progressively increased using an expansion ratio of 10%.

Away from the walls, the mesh resolution is based on both turbulent and acoustic criteria [22]. Concerning the acoustics, the chosen characteristic length of the tetrahedra ensures that at least 13 points per wavelength are used up to 15 kHz. Propagation at those frequencies is ensured up to one chord length away from the blades and the vanes. Concerning the turbulence resolution, the calculation of the autocorrelation of the axial velocity in the inter-stage gives an estimation of the Taylor-micro scale and of the integral length scale. The mesh size is 45 times larger than the Taylor micro-scale and 5 times smaller than the integral length scale.

Figure 2 illustrates the mesh refinements used to propagate acoustics up to 15 kHz, over one chord length upstream and downstream of the fan/OGV stage.

Fig. 2 Radial cut of the computational domain colored by the element caracteristic size.

III. Results

The proper convergence of the statistics enables the detailed analysis of the flow. Whenever available, the comparison with the experimental measurements is made. A modal decomposition of the acoustic signal is then analyzed and a low frequency noise emission is uncovered and analyzed.

A. Verification and comparison to experimental results

To ensure a proper physical analysis, temporal convergence is necessary. Multiple criteria can be used to ensure convergence is reached. One must ensure that mass-flow rate is well converged in order to compare averaged results with experimental data. Figure 3 highlights the evolution of the mass flow rate in time. Only the rotations 7 to 23 are represented. Starting from rotation 10 the mass flow rate is no longer evolving.

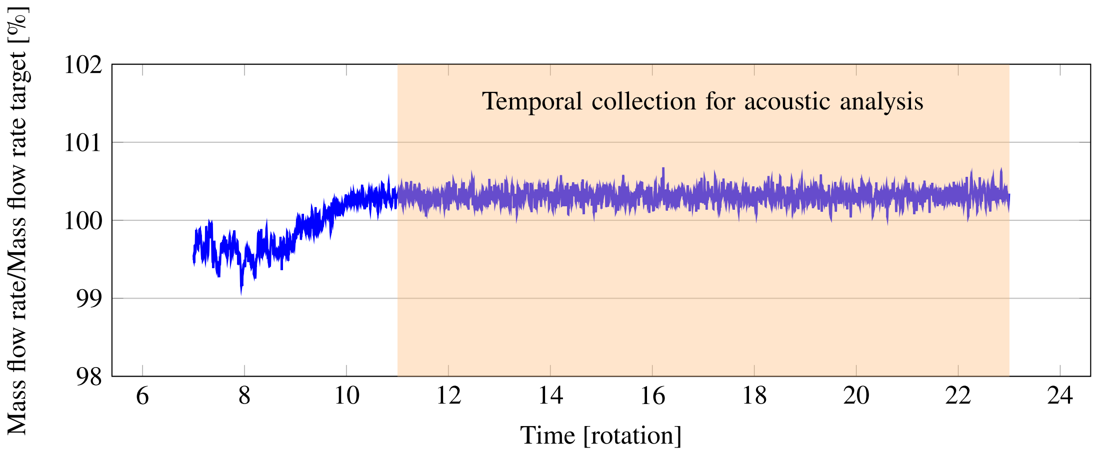

Fig. 3 Time evolution of the mass flow rate against the target value. The first seven revolutions correspond to the initialization of the solution with a Lax-Wendroff scheme. The TTGC scheme is used from rotation 7 to the end of the simulation. The twelve last rotations are used for the acoustic analysis.

The validation of the averaged results with the experimental campaign is presented in figures 4a and 4b. The time-averaged LES results are obtained by using 33,000 snapshots per rotation for 12 full rotations of the rotor. Figure 4a places the performance of the periodic sector LES on the experimental characteristic curve. The experimental characteristic curve refers to the nominal speed line (100Nn). The reference operating point extracted from the experimental characteristic curve is represented with ●, while the periodic LES is marked with ⊗. The LES lies correctly on the experimental characteristic curve. Figure 4b compares the radial profiles of total pressure ratio and total temperature ratio at the stator exit plane, two chords downstream of the vanes' trailing edge. Both quantities follow the same trend, and a good agreement is observed between the LES and the experiment. The only significant difference occurs in total temperature near the casing.

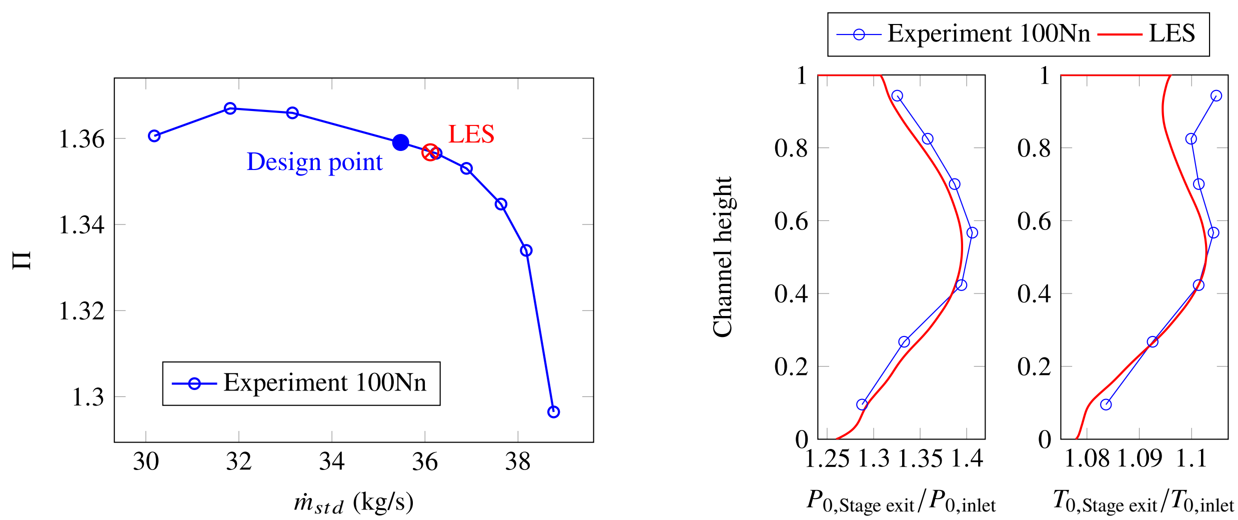

(a) Characteristic

(b) Radial profiles

Fig. 4 Comparison of periodic sector LES and experimental measurements. (a) Characteristics (total pressure ratio vs mass-flow rate). (b) Radial profiles of total pressure ratio and total temperature ratio in the stage exit plane, two chords downstream of the trailing edge of the vanes.

B. Mean and instantaneous results

Several blade-to-blade views are provided in figure 5. Figures 5a and 5c depict the average relative Mach number and the average Mach number at 80% of the span around the rotor and stator respectively. The sonic line is highlighted in white. The supersonic region extends up to 40% of the chord on the suction side of the rotor blade. Figure 5b represents the average relative Mach number at 99% of the rotor span. The flow is entirely supersonic upstream of the rotor blades but transitions to a subsonic regime in the tip leakage flow.

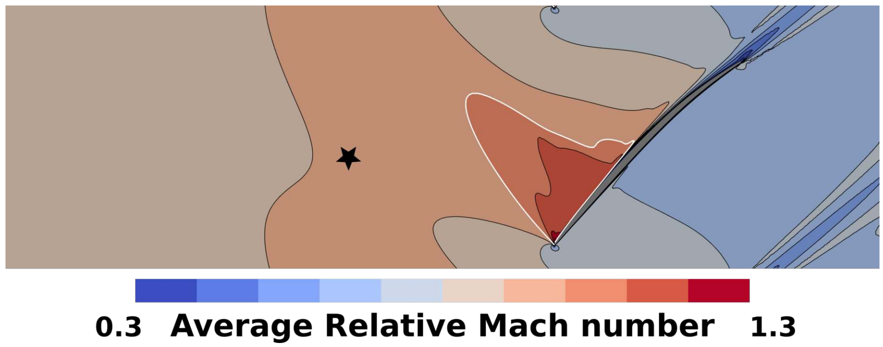

(a) Rotor 80% of span

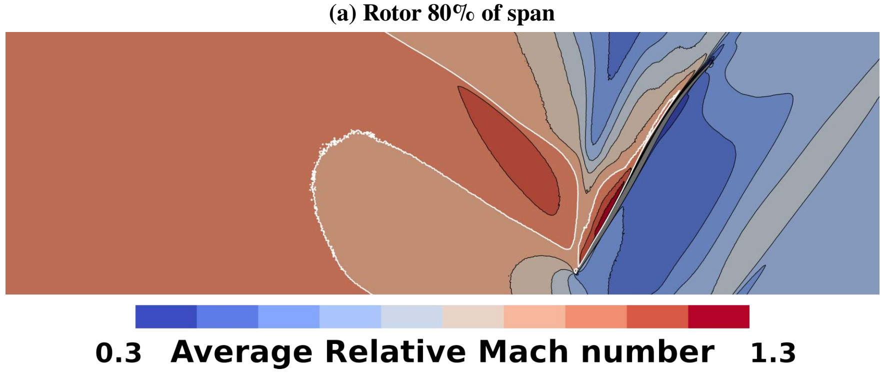

(b) Rotor 99% of span

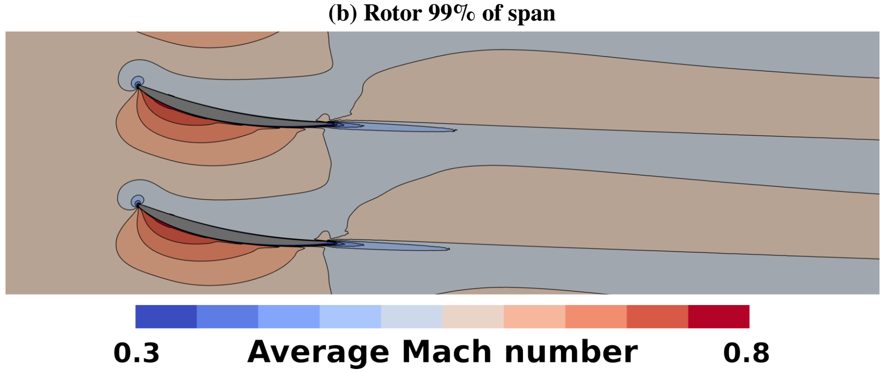

(c) Stator 80% of span

Fig. 5 Average relative Mach number at different radial positions in the rotor domain (a, b) and the stator domain (c). A time signal is extracted from a stationary probe indicated by a star in figure (a).

Figure 6 shows an isosurface of the Q-criterion colored by the relative Mach number. One can notice the laminar to turbulent transition of the suction side boundary layer occurring roughly at 20% of the chord up to 60% of the span. In the tip region, the transonic flow triggers an early transition almost at the leading edge.

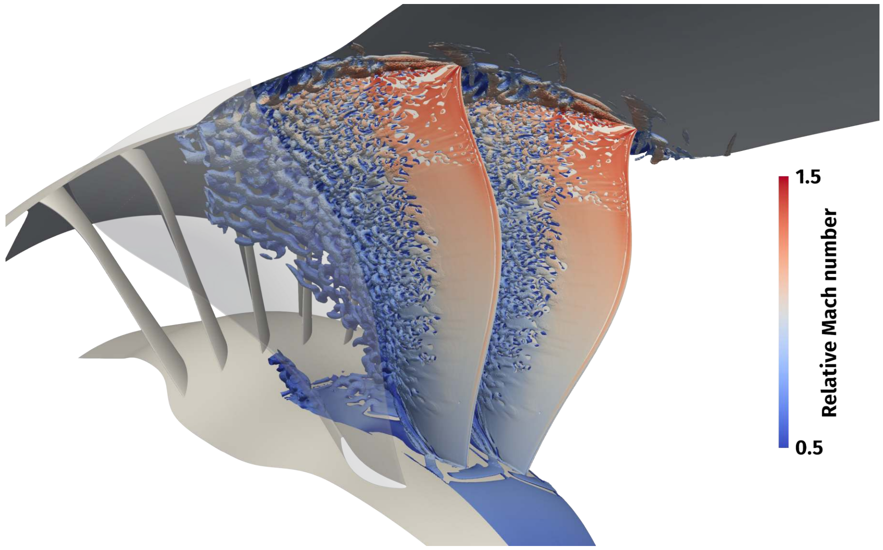

Fig. 6 Isosurface of the Q-criterion ($Qc^2/U_0{}^2 = 10$) colored by the relative Mach number

C. Spatio-temporal analysis

Figure 7 shows the power spectral density of pressure fluctuation at a stationary probe in the absolute frame of reference and located one chord upstream of the rotor blades at 80% of channel height. The spectrum amplitude is averaged using Welch's method with 7 segments and an overlap of 50%. The spectral resolution is $\Delta f = 61$ Hz. A rectangular window is used for each temporal segment. Tonal noise at the blade passing frequency (BPF) and harmonics can be easily identified, as well as a broadband component. An unexpected low frequency hump can also be noticed, with power levels comparable to that of the first harmonics of the BPF. This low frequency hump lies between 750 Hz and 1200 Hz, or 0.25 BPF and 0.4 BPF.

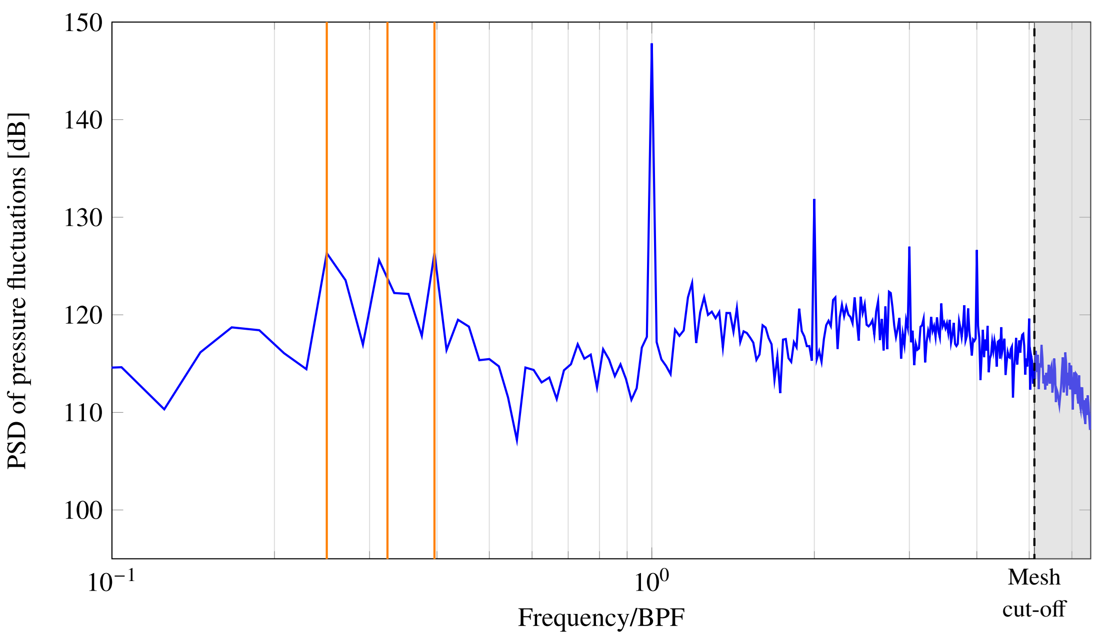

Fig. 7 Power spectral density of the pressure fluctuations at the stationary probe one chord upstream the rotor blades at 80% of the span. The blade passing frequency equals 2933 Hz. The orange lines are positioned at 0.25 BPF (750 Hz), 0.33 BPF (975 Hz) and 0.4 BPF (1200 Hz).

A dynamic mode decomposition has been performed in order to filter the flow and investigate the low frequency component [23]. The dataset considered contains 990 instantaneous 3D solutions of the rotor domain, on a coarser grid than the computational grid for low-storage purpose. Sampling was performed at 60 kHz (50 times the highest frequency of interest at 1200 Hz) for 3 full rotations of the fan (at least 12 periods of the phenomenon of interest at 750 Hz). Figure 8 shows the reconstructed pressure fluctuations filtered at 750 Hz, at four successive instants. The simulation time elapsed between the first snapshot (top) and the last snapshot (bottom) represents 75% of a 750 Hz period. Dashed lines crossing all the pictures suggests the motion of a mode in time. Fluctuations are propagating towards the inlet. This mode at 750 Hz does not present any azimuthal variation, but present a node in the radial direction. In the absolute frame of reference, one could expect to observe an acoustic mode at the frequency $f = 750$ Hz with an azimuthal order $m = 0$ and a radial order $n = 1$. In the inlet duct, near the casing, localized fluctuations are associated with the crossing of the shock waves from the adjacent blades. In the inter-stage, turbulent fluctuations from the tip-leakage flow are visible.

Analyzing the acoustic field with DMD however presents some limitations. Indeed, at a given frequency, DMD will always provide the most energetic mode. To prevent the analysis from being blinded by the significant noise emissions originating from the rotor blades, one needs to turn to a proper acoustic modal analysis. Also, the DMD is carried out in the relative frame of reference: the most energetic mode identified by the DMD in the rotor domain is associated with the vane passing frequency, and the blade passing frequency cannot be observed. Moreover, while one would expect the radial nature of the acoustic modes to be preserved from one frame of reference to another, the azimuthal behavior remains unclear. The purpose of the next section is to perform this acoustic modal analysis.

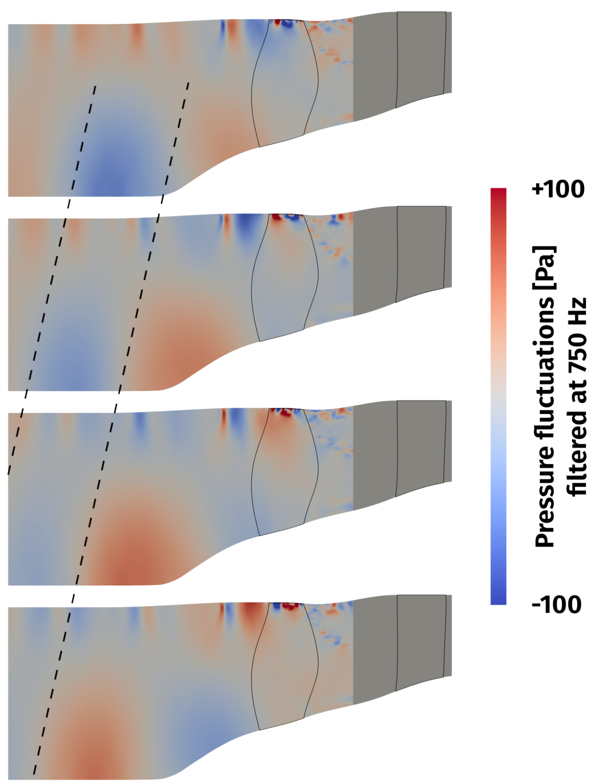

Fig. 8 Cut at $\theta = 0°$ in the rotor domain, colored by the pressure fluctuations filtered at 750 Hz using DMD, at four successive instant equally spaced within a full period. Leading edges and trailing edges of rotor blades and stator vanes are represented with black solid lines. The range of the filtered pressure fluctuations extents from -100 to 100 Pa.

D. Modal analysis

Methodology

The low frequency phenomenon is further investigated using an acoustic duct-mode decomposition. The decomposition is performed using the triple planes mode-matching strategy developed by Ovenden and Rienstra [24]. This approach also to take into account a slowly varying duct cross-section.

The flow is assumed to be uniform and axial. The pressure field is Fourier-decomposed in frequency and azimuthal order:

$$p(x, r, \theta, t) = \int_0^\infty \sum_{m=-\infty}^{+\infty} p_{\omega,m}(x, r) \exp(i\omega t - im\theta) \mathrm{d}\omega \tag{1}$$

with $p_{\omega,m}$ the Fourier component at the frequency $(\omega/2\pi)$ and azimuthal order (m).

Each component is a wave propagating in a duct with a slowly varying section and mean flow along the axial position. Each component can be written as the summation of left- and right-running modes:

$$p_{\omega,m}(x, r) = \sum_{n=0}^{+\infty} A_{\omega,m,n}{}^{\pm} \psi_{m,n}{}^{\pm}(x, r) \exp\left(-i \int_{x_0}^{x} k_{\omega,m,n}{}^{\pm}(\varepsilon\sigma) \mathrm{d}\sigma\right) \tag{2}$$

where $\psi_{m,n}\pm$ denotes the radial functions of right-running (+) and left-running (−) modes of azimuthal order m and radial order n. $A_{\omega,m,n}{}^{\pm}$ is the amplitude of the acoustic mode (m, n) at the frequency ω and computed for the plane located at x_0. The wavenumber $k_{\omega,m,n}{}^{\pm}$ denotes the axial wavenumber. The integral and the control parameter ε take into account the slow variations of the geometry and mean flow in the axial direction. The axial wavenumber satisfies the dispersion relation:

$$k_{\omega,m,n}{}^{\pm} = \frac{M_x \omega/c}{1 - M_x{}^2} \pm \frac{1}{1 - M_x{}^2} \sqrt{\left(\frac{\omega}{c}\right)^2 - (1 - M_x{}^2)\kappa_{mn}^2} \tag{3}$$

with c the speed of sound, M_x the axial Mach number and κ_{mn} the duct constant imposed by the hard-wall boundary conditions at the hub and shroud. The axial wavenumber can be a complex number with $\mathrm{Im}(k_{\omega,m,n}{}^{\pm}) \neq 0$. In this case the duct mode amplitude will decrease exponentially with axial position for right-running modes, and increase exponentially with axial position for left-running modes. The mode-matching strategy relies on performing the full decomposition on each axial plane, then for each frequency ω, for each azimuthal order m finding all the amplitudes $A_{\omega,m,n}{}^{\pm}$ that satisfy the decomposition while taking into account the axial changes from one plane to another. The full methodology relies on hermitian matrices that substitute the minimization process by a linear system that is easily solved using standard procedures. More details on this methodology can be found in the original paper of Ovenden and Rienstra.

Performing this full decomposition has multiple advantages. It allows to fully describe the acoustic modes in a duct, quantify levels of reflection at the inlet and outlet boundaries in the simulation, identify modes that propagate (cut-on) and modes that vanish (cut-off) and describe left- and right-running modes in the inter-stage.

In this study, the original triple plane approach is generalized to any number of planes for the mode-matching strategy.

Three regions of interest are identified: upstream of the rotor, downstream of the stator, and the inter-stage. Several axial cuts are extracted in those regions: six upstream of the rotor, ten in the inter-stage, and seven downstream of the stator vanes. The planes are represented in Figure 9. The thick orange planes are those where the modal coefficients are calculated and set the nature of an acoustic duct mode. Cuts are extracted at a frequency of f_s = 96.8 kHz, which corresponds to 528 samples per rotation or 33 samples per blade passage. The axial cuts are directly stored on a structured cylindrical grid with a resolution of n_θ points in the azimuthal direction and n_r points in the radial direction. Since the axial planes must be extracted in the absolute frame of reference, the azimuthal resolution must match the angular increment of the considered frequency sampling: $2\pi/n_\theta = \Omega/f_s$. In the present case, 33 points are used in the azimuthal direction (for a sector of $2\pi/16$). The radial resolution is chosen so that the radial and the azimuthal spacings at midspan are matching. It corresponds to approximately 200 points in the radial direction.

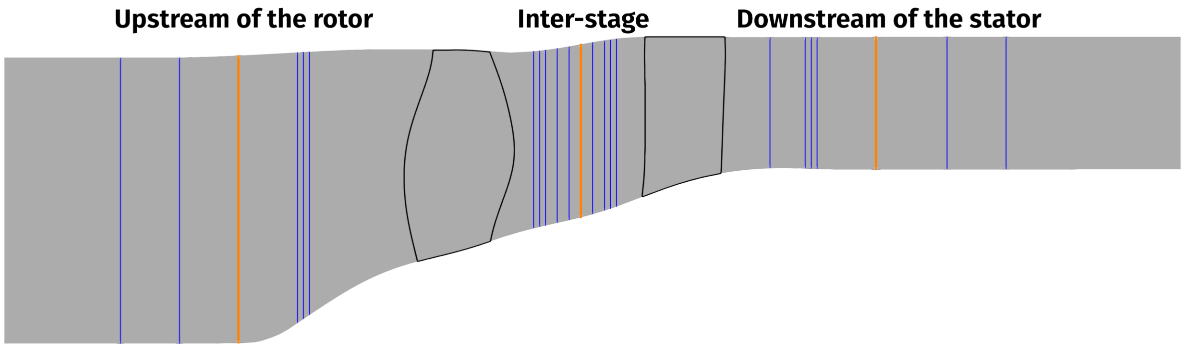

Fig. 9 Meridional cut of the entire computational domain. Contours of the rotor blades and the stator vanes are represented with black solid lines. Axial plane locations are represented with blue solid lines. The main planes of interest are colored in orange.

The recording is performed over 12 full rotations. The duct mode coefficients are computed and amplitudes averaged using Welch's method. Seven temporal windows are used with an overlap of 50%. Therefore, each segment represents a signal of 3 full rotations leading to a spectral resolution of $\Delta f = 61$ Hz, or $1/48$ the blade passing frequency. A rectangular window is used for the temporal Fourier transform. The results are presented in decibels, with a reference pressure value of 20 μPa. Due to the angular periodicity of the dataset, it is expected to observe azimuthal modes that are multiples of 16 only. Figure 10 illustrates the spatial distributions of some modes on an axial cut upstream of the rotor blade. The region within the thick line corresponds to the $2\pi/16$ angular extent. The periodic nature of the simulation imposes to have a whole number of periods in the azimuthal direction.

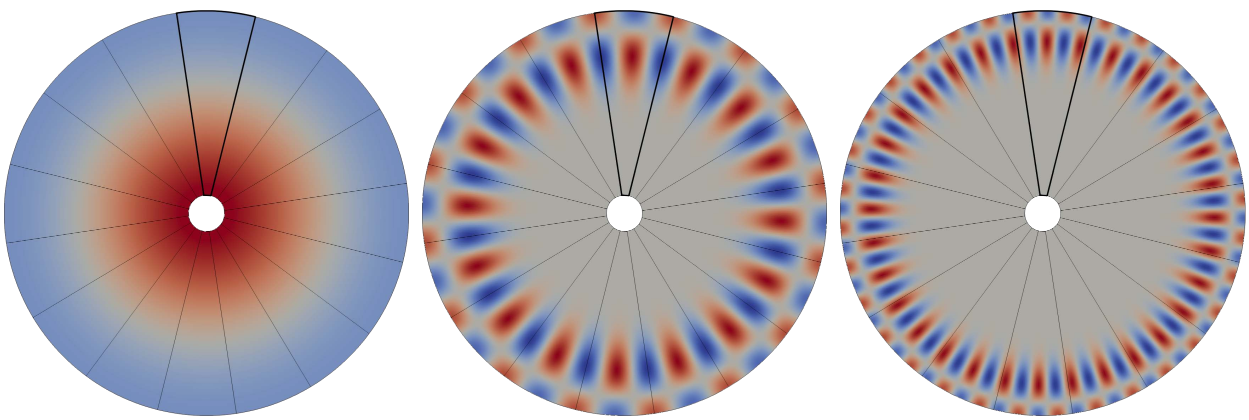

(a) Azimuthal order: 0 **(b) Azimuthal order: 16** **(c) Azimuthal order: 32**

Fig. 10 Examples of spatial distributions of acoustic duct modes on an axial cut for upstream the rotor. The region within the black thick lines represents an extent of the periodic domain. Radial order is set to 1. Range scale is arbitrary.

Results upstream of the rotor blades

The decomposition can be used to identify the level of reflection at the inlet boundary condition (NSCB). Figure 11 presents the summations of all azimuthal and radial modes for both left-running and right-running modes for the entire frequency range. Levels of right-running modes are approximately 10 dB lower than levels of left-running modes suggesting, low levels of reflection near the inlet.

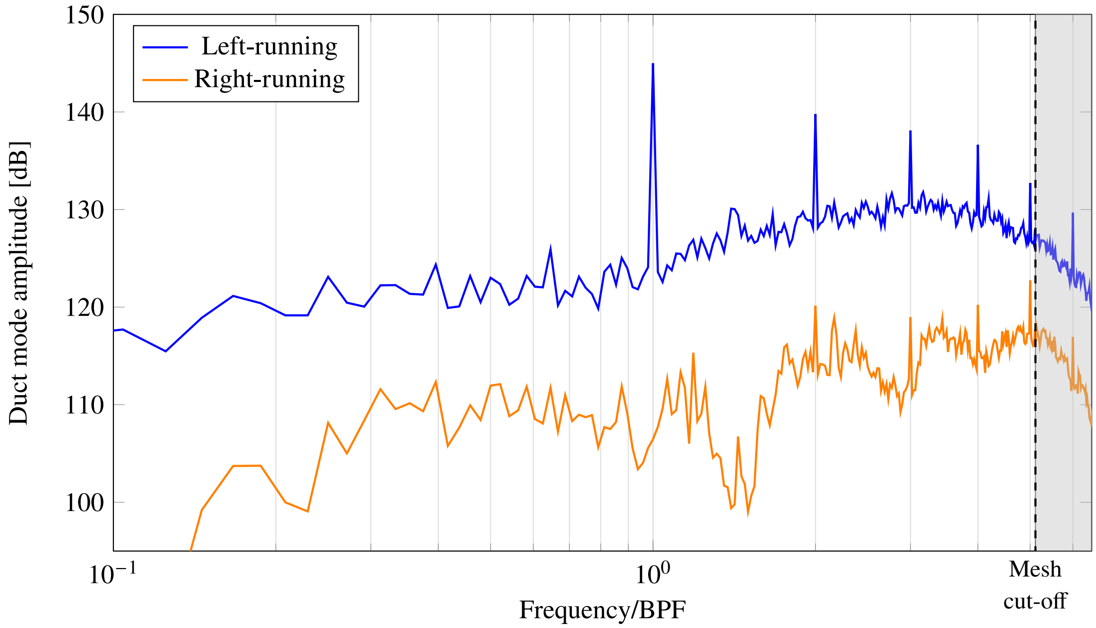

Fig. 11 Frequency spectrum comparing the left- and right-running modes upstream of the rotor blade.

The duct-mode decomposition also allows separating the modes that are cut-off and the ones that propagate. Figure 12 compares the levels of all the left-running modes and the levels of the left-running modes that propagates. The levels of propagating modes are lower than levels of all modes over the whole frequency range, but remain close to the levels including all modes (except at the BPF). This can be explained by the nature of the duct that is cylindrical at the inlet. A difference of 25 dB can be noticed at the BPF because the duct modes responsible for this tonal component, resulting from the interaction of the fan wake with the OGV, known as the Tyler & Sofrin [**?**] interaction modes are cut-off. Figure 13 shows the levels of the left-running modes ($m = 0, n = 0$), ($m = 16, n = 0$), ($m = 32, n = 0$) and ($m = 48, n = 0$) for the entire frequency range. The dashed segments represent the frequency range where the modes are cut-off, while the solid lines represent frequency range where they are cut-on. It can be noticed that the highest mode amplitude is obtained at the BPF which corresponds to a corotating ($m = 16$) and evanescent. The same is observed for the harmonics of the BPF and the corresponding azimuthal mode order. This result can explain the difference observed in Figure 12. It should be noted the values of the BPFs are close, but slightly lower than the cut-off frequency of an azimuthal mode: the damping exists but the associated characteristic damping length is large compared to the chord length.

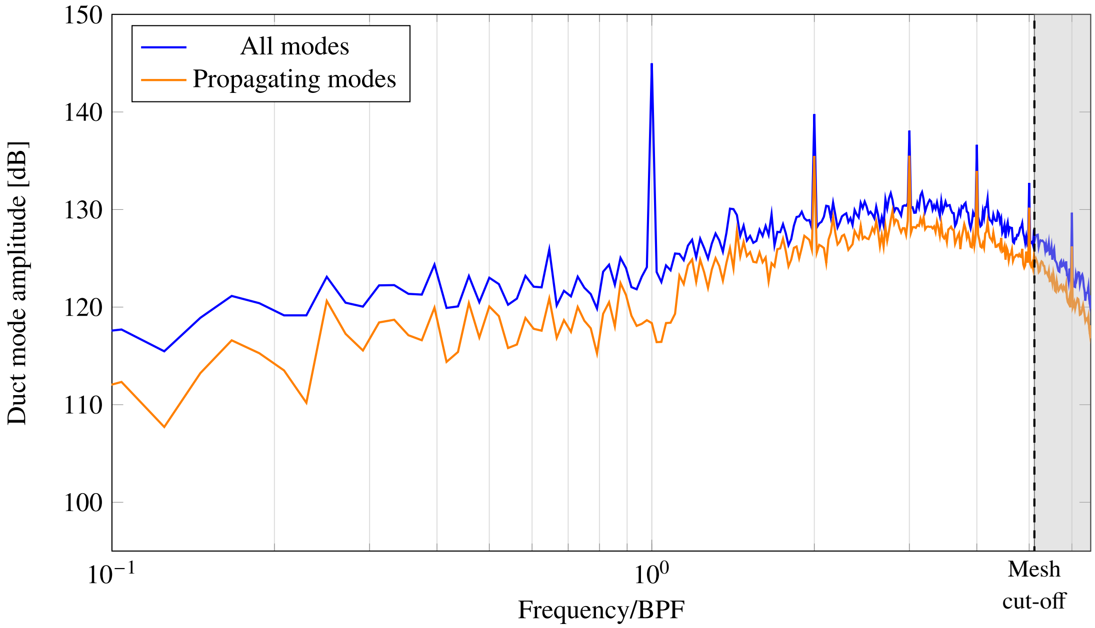

Fig. 12 Frequency spectrum of the left-running modes upstream of the rotor: all modes vs propagating modes only.

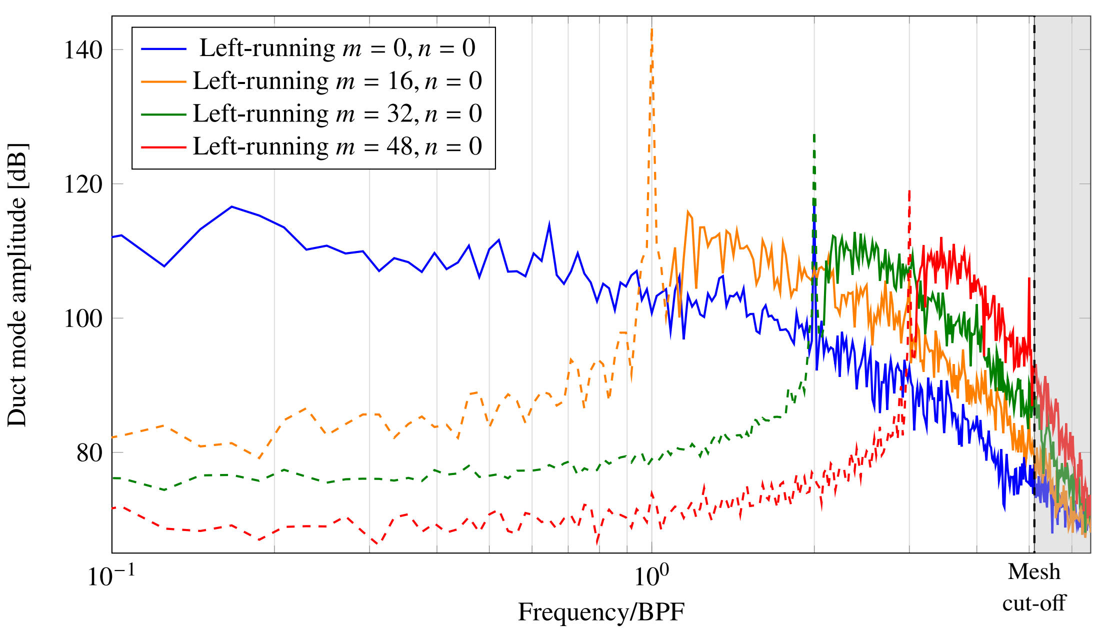

Fig. 13 Frequency spectra of acoustic modes of different azimuthal order ($m = 0, 16, 32, 48$) **for the same radial order** ($n = 0$) **upstream of the rotor. .**

The DMD performed in the previous section suggested the existence of an acoustic duct mode at low frequency (around 750 Hz) with $m = 0$ and $n = 1$. Figure 14 presents the levels of the left-running and right-running acoustic duct modes, for the entire frequency range, with $m = 0$ and $n = 1$. The levels of right-running modes are 10 dB lower than levels of left-running modes here has well. High-levels of left-running modes can be identified in the range from 0.25 BPF to 0.42 BPF (from 750 Hz to 1200 Hz). All of those modes are cut-on and, therefore, will propagate in all the computational domain. Those levels are comparable to those of the peak at the frequency 2 BPF, where the modes $m = 0$ that corresponds to a Tyler & Sofrin interaction mode between the rotor blades and stator vanes [**?**]. Three different DMD fields of the pressure fluctuations in the range of identified frequencies are represented Figure 15. The DMD highlight the nature of the acoustic modes with $m = 0$ and $n = 1$. Considering the inter-stage region, between the rotor and the stator, while an acoustic mode with $m = 0$ and $n = 1$ is identifiable at 1200 Hz in Figure 8, the nature of the acoustic modes for lower frequencies remains unclear.

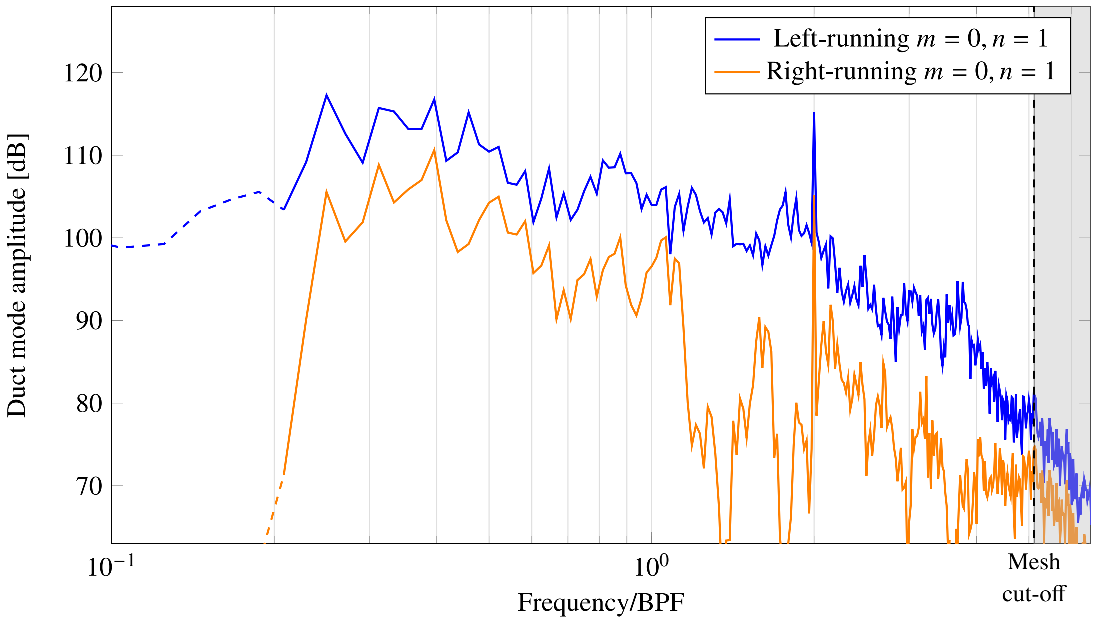

Fig. 14 Frequency spectrum of the left- and right-running acoustic duct modes with azimuthal order $m = 0$ and radial order $n = 1$, upstream of the rotor blades.

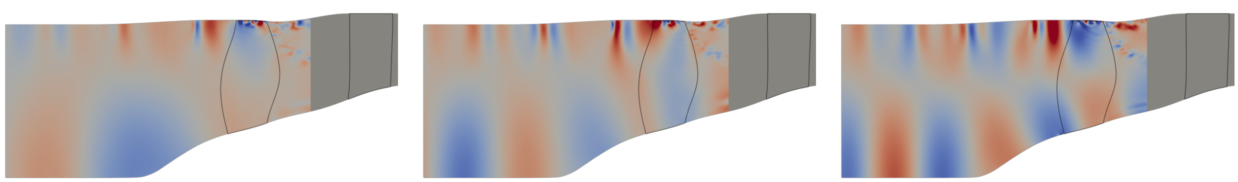

(a) Filtered at 750 Hz **(b) Filtered at 975 Hz** **(c) Filtered at 1200 Hz**

Fig. 15 Cut at $\theta = 0°$ in the rotor domain, colored by the pressure fluctuations filtered at several low frequencies using DMD. Leading edges and trailing edges of rotor blades and stator vanes are represented with black solid lines. The range of the filtered pressure fluctuations extents from -100 to 100 Pa.

Results downstream of the stator vanes

The low frequencies acoustic duct modes of azimuthal order $m = 0$ and radial order $n = 1$ are also investigated downstream of the stator vanes. Figure 16 presents the levels of left-running and right-running acoustic duct modes for the entire frequency range, with $m = 0$ and $n = 1$, downstream the stator vanes. Reflexion are 10 dB lower for the entire frequency range. In this region, the duct geometry and mean flow properties make acoustic duct modes of azimuthal order $m = 0$ and radial order $n = 1$ evanescent when their frequency is below 0.44 BPF, or 1300 Hz. The low frequency phenomenon identified upstream of the fan cannot propagate downstream of the stator vanes.

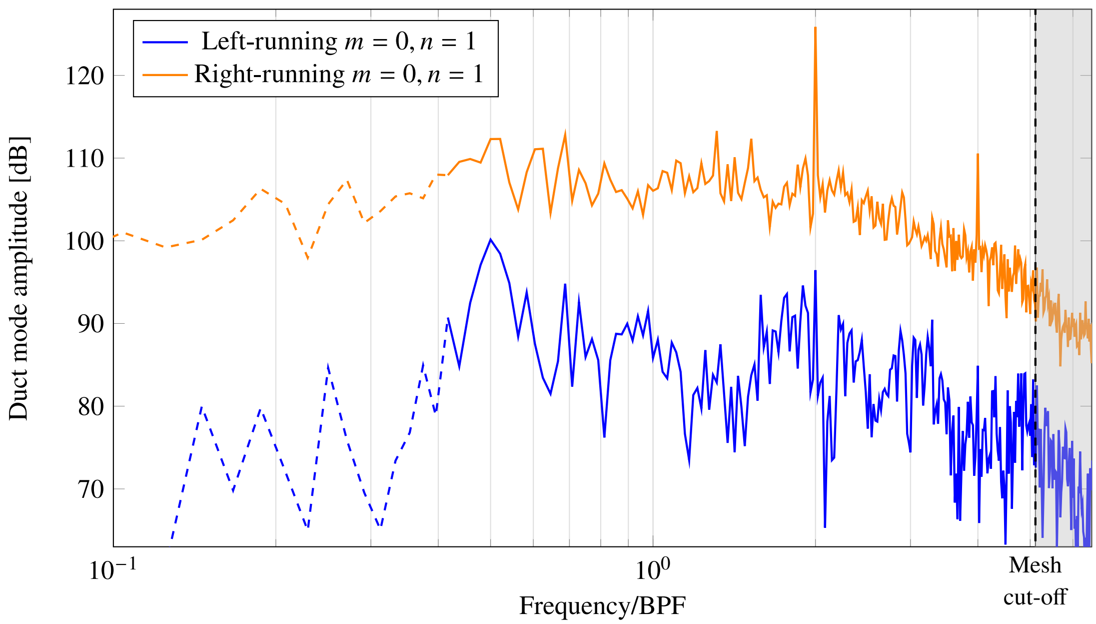

Fig. 16 Frequency spectra of the left- and right-running acoustic duct modes with azimuthal order $m = 0$ and radial order $n = 1$, downstream of the stator vanes.

Results in the inter-stage

The low frequencies acoustic duct modes of azimuthal order $m = 0$ and radial order $n = 1$ are investigated next in the inter-stage. Figure 17 presents the levels of left-running and right-running acoustic duct modes for the entire frequency range, for $m = 0$ and $n = 1$, in the inter-stage. In this region, the duct geometry and mean flow properties make acoustic duct modes of azimuthal order $m = 0$ and radial order $n = 1$ evanescent when their frequency is below 0.35 BPF, or 1000 Hz. Yet given their wavelengths, cut-off modes can still exist at significant levels in the inter-stage region. For the left-running modes (from stator vanes to the rotor blades), a peak near 0.4 BPF can be identified and is compatible with the DMD observation in Figure 15c. For lower frequencies, results are not that clear. A hump is visible at 0.3 BPF for right-running modes but is close to the cut-off frequency. One should keep in mind that the inter-stage distance is twice as small as the characteristic damping length of that mode suggesting that the mode could interact with the stator vanes. The amplitudes of this structural duct mode at the given frequencies are not negligible for both left- and right-running modes. It should be noted that the characteristic time travel of acoustic between the stator leading edges and the supersonic root at the suction side of the rotor blade back to the leading edge of the vanes lies around 800 Hz. The characteristic frequency associated with acoustic traveling between the trailing edge of the blades and the leading edge of the vanes falls near 1250 Hz.

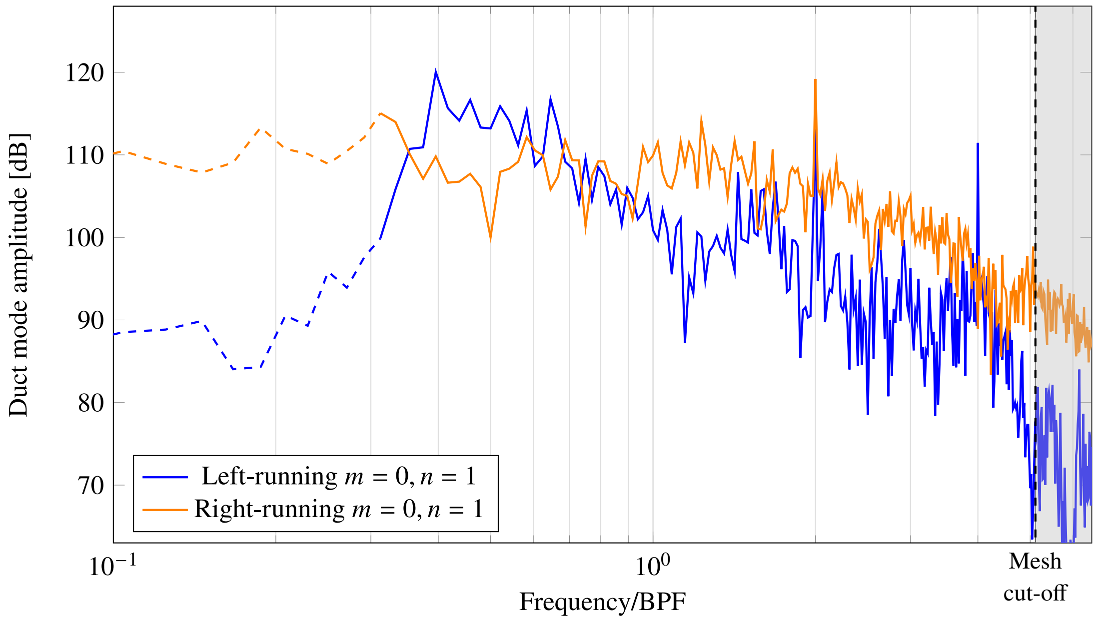

Fig. 17 Frequency spectra of the left- and right-running acoustic duct modes, with azimuthal order $m = 0$ and radial order $n = 1$, in the inter-stage.

IV. Conclusion

In this study, a large eddy simulation of a periodic sector fan/OGV stage was conducted at transonic speeds. Averaged results from the simulation demonstrated a good agreement with experimental measurements. The simulation were shown to be well-converged.

The acoustic analysis was performed using time signals spanning over twelve rotations. Low frequencies phenomena were investigated through dynamic mode decomposition and mode-matching strategy for acoustic in duct. The mode matching analysis were conducted at multiple locations: upstream of the blades, downstream of the vanes, and at the inter-stage.

The modal structure of the low frequencies phenomena was successfully described to be homogenous in azimuthal direction and first order radial. The frequency range indicated that acoustic modes can propagate upstream of the rotor blade but are unable to propagate downstream of the stator vanes. This observation suggests a directional propagation characteristic of the acoustic modes within the fan/OGV sector. Additionally, the interstage decomposition and characteristic frequencies of the acoustic modes hinted at the potential existence of a trapped mode, which requires further investigation.

To advance our understanding, several future investigations are recommended. These include an investigation of others structural modes in the inter-stage to identify the most significant contributors to the acoustic, and describe the interactions between the rotor and the stator. The large eddy simulation of the rotor alone should shed more light on this phenomenon.

Acknowledgments

The authors recall that the development of the fan was conducted within the PhD thesis of Valdo Pages and supervised by Stephane Aubert, Pascal Ferrand, and Pierre Duquesne from LMFA, as well as Laurent Blanc from LTDS. The final design was developed in close collaboration with Safran Aircraft Engines.

The authors particularly thank Jean Al-Am for his turbomachinery LES expertise, and the advice given the past four years.

The present work was supported by CIRT (Consortium Industrie-Recheche en Turbomachines) in the frame of the *Sonos* project.

The computational resources for the LES were provided by GENCI (IRENE, project number A0162A05039). This

work was granted access to the HPC resources of PMCS2I (Pôle de Modélisation et de Calcul en Sciences de l'Ingénieur et de l'Information) of École Centrale de Lyon, Écully, France. Post-processing were performed using the python library Antares (release 2.3.0).

References

[1] Tyler, J. M., and Sofrin, T. G., "Axial Flow Compressor Noise Studies," , ???? https://doi.org/10.4271/620532, URL https://www.sae.org/publications/technical-papers/content/620532/, ISSN: 0148-7191, 2688-3627.

[2] Moreau, S., "Turbomachinery Noise Predictions: Present and Future," Vol. 1, No. 1, ????, pp. undefined–undefined. https://doi.org/10.3390/acoustics1010008, URL https://www.mendeley.com/catalogue/fc9a5913-1bab-368a-9369-e04c6dd5c852/, number: 1.

[3] Al-Am, J., Clair, V., Giauque, A., Boudet, J., and Gea-Aguilera, F., "Aeroacoustic analysis of the tip-leakage flow of an ultrahigh bypass ratio fan stage," *Physics of Fluids*, Vol. 35, No. 4, ????, p. 047104. https://doi.org/10.1063/5.0146143, URL https://doi.org/10.1063/5.0146143.

[4] Amiet, R. K., "Acoustic radiation from an airfoil in a turbulent stream," *Journal of Sound and Vibration*, Vol. 41, No. 4, ????, pp. 407–420. https://doi.org/10.1016/S0022-460X(75)80105-2, URL https://www.sciencedirect.com/science/article/pii/S0022460X75801052.

[5] Al-Am, J., Giauque, A., Clair, V., Boudet, J., and Gea-Aguilera, F., "Direct-Noise of an Ultrahigh-Bypass-Ratio Turbofan: Periodic-Sector vs Full-Annulus Large-Eddy Simulations," ????, pp. 1–15. https://doi.org/10.2514/1.j063596, URL https://arc.aiaa.org/doi/10.2514/1.J063596, publisher: American Institute of Aeronautics and Astronautics (AIAA).

[6] Pagès, V., Duquesne, P., Ottavy, X., Ferrand, P., Aubert, S., Blanc, L., and Brandstetter, C., "UHBR Open-test-case fan ECL5/Catana, Part 2: Mechanical and aeroelastic stability analysis," *European Conference on Turbomachinery Fluid Dynamics and Thermodynamics*, European Turbomachinery Society, 2021. https://doi.org/10.29008/ETC2021-625, URL https://www.euroturbo.eu/publications/proceedings-papers/ETC2021-625/.

[7] Pagès, V., Duquesne, P., Aubert, S., Blanc, L., Ferrand, P., Ottavy, X., and Brandstetter, C., "UHBR Open-Test-Case Fan ECL5/CATANA," *IJTPP*, Vol. 7, No. 2, 2022, p. 17. https://doi.org/10.3390/ijtpp7020017, URL https://www.mdpi.com/2504-186X/7/2/17.

[8] Brandstetter, C., Pages, V., Duquesne, P., Ottavy, X., Ferrand, P., Aubert, S., and Blanc, L., "UHBR Open-test-case fan ECL5/Catana, Part 1: Geometry and aerodynamic performance," *European Conference on Turbomachinery Fluid Dynamics and Thermodynamics*, European Turbomachinery Society, 2021. https://doi.org/10.29008/ETC2021-626, URL https://www.euroturbo.eu/publications/proceedings-papers/ETC2021-626/.

[9] Schonfeld, T., and Rudgyard, M., "Steady and Unsteady Flow Simulations Using the Hybrid Flow Solver AVBP," *AIAA Journal*, Vol. 37, No. 11, 1999, pp. 1378–1385. https://doi.org/10.2514/2.636, URL https://arc.aiaa.org/doi/10.2514/2.636, publisher: American Institute of Aeronautics and Astronautics.

[10] Rai, M. M., and Madavan, N. K., "Multi-Airfoil Navier–Stokes Simulations of Turbine Rotor–Stator Interaction," *Journal of Turbomachinery*, Vol. 112, No. 3, 1990, pp. 377–384. https://doi.org/10.1115/1.2927670, URL https://asmedigitalcollection.asme.org/turbomachinery/article/112/3/377/436877/MultiAirfoil-NavierStokes-Simulations-of-Turbine.

[11] Moreau, S., "Turbomachinery-related aeroacoustic modelling and simulation," *17th International Conference on Fluid Flow Technologies*, 2018.

[12] Al Am, J., Clair, V., Giauque, A., Boudet, J., and Gea-Aguilera, F., "Direct noise predictions of fan broadband noise using LES and analytical models," *28th AIAA/CEAS Aeroacoustics 2022 Conference*, American Institute of Aeronautics and Astronautics, Southampton, UK, 2022. https://doi.org/10.2514/6.2022-2882, URL https://arc.aiaa.org/doi/10.2514/6.2022-2882.

[13] Wang, G., Duchaine, F., Papadogiannis, D., Duran, I., Moreau, S., and Gicquel, L. Y. M., "An overset grid method for large eddy simulation of turbomachinery stages," *Journal of Computational Physics*, Vol. 274, 2014, pp. 333–355. https://doi.org/10.1016/j.jcp.2014.06.006, URL https://www.sciencedirect.com/science/article/pii/S0021999114004136.

[14] Papadrakakis, M., Oñate, E., and Schrefler, B., "O-PALM: AN OPEN SOURCE DYNAMIC PARALLEL COUPLER," 2011.

[15] Colin, O., and Rudgyard, M., "Development of High-Order Taylor–Galerkin Schemes for LES," *Journal of Computational Physics*, Vol. 162, No. 2, 2000, pp. 338–371. https://doi.org/10.1006/jcph.2000.6538, URL https://linkinghub.elsevier.com/retrieve/pii/S0021999100965380.

[16] Nicoud, F., Toda, H. B., Cabrit, O., Bose, S., and Lee, J., "Using singular values to build a subgrid-scale model for large eddy simulations," *Physics of Fluids*, Vol. 23, No. 8, 2011, p. 085106. https://doi.org/10.1063/1.3623274, URL https://doi.org/10.1063/1.3623274.

[17] Poinsot, T. J., and Lelef, S. K., "Boundary conditions for direct simulations of compressible viscous flows," *Journal of Computational Physics*, Vol. 101, No. 1, 1992, pp. 104–129. https://doi.org/10.1016/0021-9991(92)90046-2, URL https://www.sciencedirect.com/science/article/pii/0021999192900462.

[18] Schmitt, P., Poinsot, T., Schuermans, B., and Geigle, K. P., "Large-eddy simulation and experimental study of heat transfer, nitric oxide emissions and combustion instability in a swirled turbulent high-pressure burner," *Journal of Fluid Mechanics*, Vol. 570, 2007, pp. 17–46. https://doi.org/10.1017/S0022112006003156, URL https://www.cambridge.org/core/journals/journal-of-fluid-mechanics/article/largeeddy-simulation-and-experimental-study-of-heat-transfer-nitric-oxide-emissions-and-combustion-instability-in-a-swirled-turbulent-highpressure-burner/D9E524C71C8AE1EA917CE85337061D42, publisher: Cambridge University Press.

[19] Cook, A. W., and Cabot, W. H., "Hyperviscosity for shock-turbulence interactions," *Journal of Computational Physics*, Vol. 203, No. 2, 2005, pp. 379–385. https://doi.org/10.1016/j.jcp.2004.09.011, URL https://www.sciencedirect.com/science/article/pii/S0021999104004000.

[20] Ducros, F., Ferrand, V., Nicoud, F., Weber, C., Darracq, D., Gacherieu, C., and Poinsot, T., "Large-Eddy Simulation of the Shock/Turbulence Interaction," *Journal of Computational Physics*, Vol. 152, No. 2, ????, pp. 517–549. https://doi.org/10.1006/jcph.1999.6238, URL https://linkinghub.elsevier.com/retrieve/pii/S0021999199962381.

[21] Bhagatwala, A., and Lele, S. K., "A modified artificial viscosity approach for compressible turbulence simulations," *Journal of Computational Physics*, Vol. 228, No. 14, 2009, pp. 4965–4969. https://doi.org/10.1016/j.jcp.2009.04.009, URL https://linkinghub.elsevier.com/retrieve/pii/S0021999109002034.

[22] Al-Am, J., Clair, V., Giauque, A., Boudet, J., and Gea-Aguilera, F., "A Parametric Study on the LES Numerical Setup to Investigate Fan/OGV Broadband Noise," *IJTPP*, 2021. URL https://www.mdpi.com/2504-186X/6/2/12.

[23] Schmid, P., "Dynamic mode decomposition of numerical and experimental data," *Journal of Fluid Mechanics*, Vol. 25, 2010, pp. 249–259. https://doi.org/10.1017/S0022112010001217.

[24] Ovenden, N. C., and Rienstra, S. W., "Mode-Matching Strategies in Slowly Varying Engine Ducts," *AIAA Journal*, Vol. 42, No. 9, ????, pp. 1832–1840. https://doi.org/10.2514/1.3253, URL https://arc.aiaa.org/doi/10.2514/1.3253.